Mesoscale Models for Effective Elastic Properties of Carbon-Black/Ultra-High-Molecular-Weight-Polyethylene Nanocomposites

Stanislav Buklovskiy[1], Kateryna Miroshnichenko[1], Igor Tsukrov[1*], Rebecca J. Thomson[2], Peder C. Solberg[2], Douglas W. Van Citters[2]

[1]University of New Hampshire, Durham, NH 03824, USA
[2]Dartmouth College, Hanover, NH 03755, USA

* Igor Tsukrov: igor.tsukrov@unh.edu

ABSTRACT

In this paper, we apply mesoscale numerical modeling to predict the effective elastic properties of conductive carbon-black/ultra-high-molecular-weight-polyethylene nanocomposites. The models are based on X-ray microcomputed tomography images. The images show that for the considered range of carbon additive weight fractions, the conductive carbon black (CB) particles are distributed around the ultra-high-molecular-weight-polyethylene (UHMWPE) granules forming a carbon-containing layer of a thickness on the order of 1-2 μm.

Finite element models of representative volume elements (RVE), incorporating the CB-containing layer, are developed. The RVEs are generated based on the size and shape statistics extracted from processed microcomputed tomography images with further incorporation of the CB-containing layer by a custom image processing code. The layer is modeled analytically as a 2-phase composite consisting of spherical CB inclusions distributed in the UHMWPE matrix. Elastic moduli predicted in the models are compared to experimental data. Results show that the numerical simulations predict effective elastic moduli within the confidence intervals of the experimental measurements up to 7.5 wt % of CB inclusions.

1. INTRODUCTION

The incorporation of carbon nanoparticles in ultra-high-molecular-weight-polyethylene (UHMWPE) provides opportunities for multifunctionality (e.g. increased electrical and thermal conductivity) and potential improvements in biomechanically relevant properties. Several studies have been performed to evaluate the dependence of the effective physical and mechanical properties of carbon-reinforced UHMWPE nanocomposites on their microstructure and manufacturing procedure, considering various types of inclusions and levels of UHMWPE crystallinity. In the studies, different types of carbon nanoparticles were successfully incorporated into the UHMWPE matrix. For example, amorphous carbon (diamond-like carbon) was

investigated as a coating for lubrication by (Rothammer et al., 2021). In their paper, carbon coating significantly increased the wear resistance of UHMWPE components used in total knee arthroplasties. Carbon nanotubes (CNT) were shown to improve the overall tribological behavior of UHMWPE (Zoo et al., 2003). It was shown that the addition of 5 wt% CNT resulted in a significant reduction of wear of UHMWPE. Carbon nanotubes were also considered by (Baliga et al., 2018) with the intention to increase the strength and wear resistance of the composite. (Favreau et al., 2022) applied equal channel angular extrusion to synthetic graphite composites of UHMWPE and observed improved ductility and work-to-failure over compression-molded controls. In (Sui et al., 2009), the addition of carbon nanofibers (CNFs) to UHMWPE has been shown to improve the crystallinity, tensile strength, and elastic modulus of the overall composite. Doping UHMWPE with carbon black (CB) nanoparticles was also considered by (Clark et al., 2006), introducing electrical conductivity and improving the overall stiffness and fracture toughness of the composite.

Both numerical and analytical approaches have been used in the modeling of UHMWPE-based composites. For example, in the context of ballistic performance, (Staniszewski et al., 2022) investigated laminates consisting of UHMWPE fibers impregnated with proprietary thermoplastic polyurethane resin under low-velocity impact loading. The material behavior was successfully modeled using FEM RVE-based approach. In the context of biomechanical applications, the damage-sensing performance of compression-molded biocompatible CNT/UHMWPE nanocomposites has been investigated by (Reddy et al., 2018). A simple theoretical model was presented to predict resistivity in both elastic and inelastic loading regimes. It was demonstrated that the addition of 0.05% CNT provided an additional 37.5% increase in toughness which would help prevent fracture of UHMWPE bearing components in prosthetic implants. (Li & Ma, 2022) presented a multiscale computational framework to predict the wear rate of UHMWPE inserts in knee joint implants. Material properties derived from uniaxial tension tests were shown to be inadequate for evaluating the wear resistance of UHMWPE under complex dynamic and cyclic loading conditions. It was also demonstrated that with the addition of semicrystalline material plasticity models at the microscale, the dynamic loading process can be simulated using the FEM procedure at the macroscale. A comprehensive review of UHMWPE-based nanocomposites can be found in (Thomson et al., 2023).

Traditional modeling approaches assume uniformly distributed inclusions in the matrix material. In the case of carbon/UHMWPE composites, however, a different microstructure is observed. The CB particles are agglomerated at high concentrations as layers around granules of UHMWPE. This paper proposes a modeling approach that is driven by such a complex microstructure. The properties of CB-containing layers are evaluated micromechanically and then utilized in the mesoscale finite element models of representative volume elements (RVE) of the overall composite. The applicability of these continuum mechanics modeling approaches to nano-reinforced polymers has been discussed in several publications, see, for example, (Armbrister et al., 2015; Zeng et al., 2008).

The rest of the paper is organized as follows. Section 2 describes the preparation and micro-computed tomography analysis (μCT) of the composite specimens. Section 3 presents the proposed 4-step modeling framework that involves the processing of μCT samples, the synthetic recreation of the microstructure of granules, the introduction of the CB-containing layer, and FE simulations of resulting volume elements. Section 4 describes the procedure for processing the results of numerical simulations and compares the results with the experimental data. In Section 5, the conclusions of this paper are listed. Some preliminary results of this study were published in conference proceedings (Buklovskyi et al., 2023) and (Miroshnichenko et al., 2023).

2. MICROSTRUCTURE OF CB/UHMWPE AS OBSERVED BY μCT

2.1. Preparation of composite specimens

This paper considers CB-reinforced UHMWPE polymers manufactured by compression molding (CM) and equal channel angular extrusion (ECAE). CM is a common manufacturing process to produce high-strength, temperature-resistant polymers, see, for example (Park & Lee, 2012). ECAE was initially proposed to change the microstructure of metals without changing the cross-section of a billet (Segal, 1999), and was later applied to polymers and polymer-based composites (Beloshenko et al., 2013; Cook et al., 2019; Favreau et al., 2022; Miroshnichenko et al., 2023; Reinitz et al., 2016; Vasylevskyi et al., 2021). For this study, specimens were manufactured using the setup shown in Fig.1. For both manufacturing techniques, the setup shown in Fig. 1 was used to produce the CB/UHMWPE samples. The dies are made of steel; the cross-section is a square 5 cm × 5 cm; the length of vertical and horizontal channels is 16.5 cm; the pressure plungers are made of aluminum.

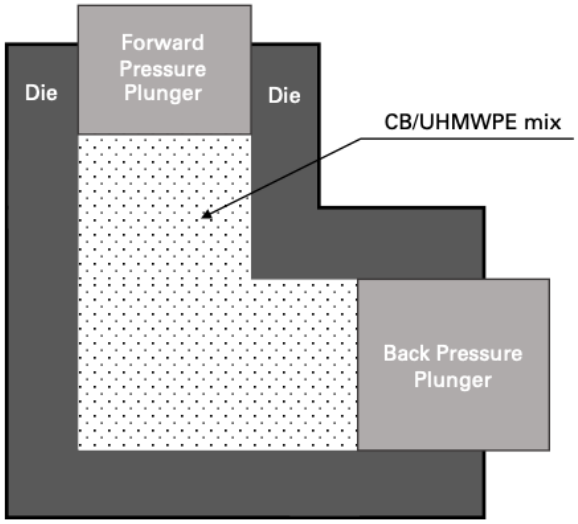

Fig. 1: A schematic of CM and ECAE setup.

First, UHMWPE GUR 1050 powder, commercially obtained from Celanese Corporation (Irving, TX), was combined with conductive CB particles obtained from Asbury Carbon (Asbury, NJ), and mechanically mixed for 25 minutes. The images illustrating UHMWPE granules (of size 50-200 μm) and the quality of mixing can be found in (Solberg, 2024). Then, the mixture was loaded into the extrusion channel and compressed under a hydrostatic pressure of 21.9 MPa with a back pressure plunger. To produce the CM samples, the mixture was consolidated at 175 oC for 2.5 hours. To produce the ECAE samples, the consolidated samples were then extruded at a rate of 0.2-0.25 mm/s, monitored by a WPS-500-MK30-P10 string potentiometer (Micro-Epsilon: Raleigh, NC). A top pressure of ~17.1 MPa was applied during the extrusion phase. A back pressure of 13.1MPa was maintained for the duration of the extrusion to ensure homogenous shearing. After extrusion or compression molding, sample billets were allowed to cool at room temperature for 24 hours. The difference in the agglomeration of CB particles around UHMWPE granules observed after CM and ECAE processes is noticeable but not substantial, as discussed in (Buklovskyi et al., 2023; Miroshnichenko et al., 2023). For the purpose of development and validation of the numerical modeling approach presented in this paper, some typical microstructures were considered and the experimental data for each wt % of CB were averaged between both processes.

2.2. μCT analysis of the composite material

In order to investigate the microstructure of the CB/UHMWPE nanocomposite, μCT studies were performed on ZEISS Xradia 610 Versa microscope with the following settings: voltage – 60 kv, power – 6.5 W, obj – 0.4X, binning – 1, exposure – 1s, filter – air. The size of the specimen was 0.49×0.5×0.52 mm^3. Some typical microstructures for different weight fractions of CB are shown in Fig.2. Grey color corresponds to UHMWPE granules; white layers around granules are associated with high concentration of carbon inclusions.

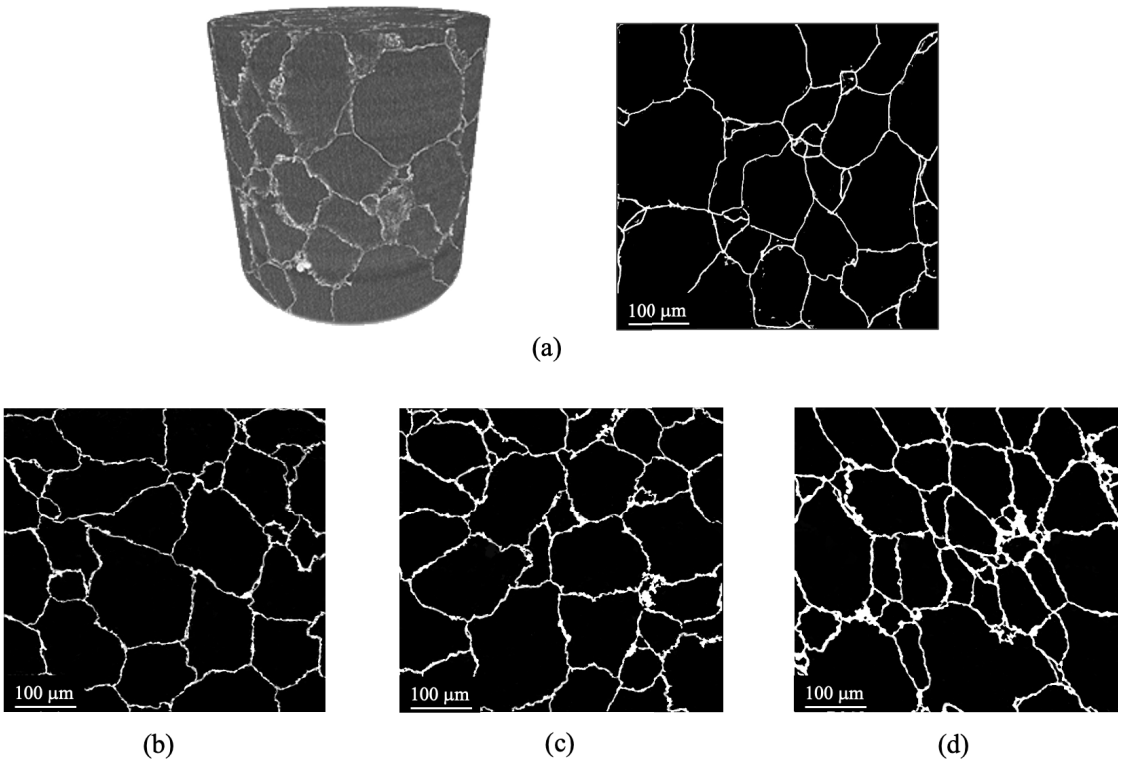

Fig.2: µCT scans of CB/UHMWPE composites: (a) 3D and 2D images of 1.5 wt% CB, (b) 1wt% CB, (c) 2.5 wt% CB, (d) 5 wt% CB.

The µCT scans were processed using ORS Dragonfly (Dragonfly 2022.2 Comet Technologies Canada Inc., Montreal, Canada) image processing software. It was observed that the granules have aspect ratios close to one and the ECAE process does not significantly change the shape of the granules, see (Miroshnichenko et al., 2023). It can also be seen that the volume fraction of white layers is higher than the total volume of carbon particles in the overall material which indicates that the white color represents a high-concentration mixture of carbon inclusions in the UHMWPE matrix. The volume fraction of CB particles (V_{CB}) in the overall composite can be found from

$$V_{CB} = \frac{W_{CB}}{W_{CB} + (1 - W_{CB})\frac{\rho_c}{\rho_m}} \tag{1}$$

where W_{CB} is the weight fraction of the inclusions in the composite, $\rho_c = 1.9$ g/cm^3 is the density of CB inclusions (Wypych, 2014), and $\rho_m = 0.93$ g/cm^3 is the density of UHMWPE (Hunt & Joyce, 2016). Then, assuming that all particles are located in the CB-containing layer, the average volume fraction of particles in the layer ($V_{c/L}$) is

$$V_{c/L} = \frac{V_{CB}}{V_L} \tag{2}$$

where V_L is the μCT-observed volume fraction of white regions. The results are summarized in Table 1. It can be seen that the volume fraction of CB in CB-containing layers varies between 27% and 46% and appears to be reaching saturation below 50%.

TABLE 1. Percent volume fractions of CB in the composite and CB-containing layer

Samples	V_{CB}	V_L	$V_{c/L}$
0.5 wt%	0.25	0.7	35
1 wt%	0.49	1.8	27
1.5 wt%	0.74	2.5	30
5 wt%	2.51	5.9	43
10 wt%	5.16	11.2	46

The average thickness of the white layers in the μCT was estimated as varying between 0.67 μm for 1 wt% to 1.98 μm for 10 wt%, see (Miroshnichenko et al., 2023). This thickness is significantly larger than the diameter of CB particles (which is approximately 35 nm, see Asbury Carbon, 2024). Thus, these layers can be treated as two-phase materials consisting of a UHMWPE matrix with CB inclusions.

3. μCT-BASED NUMERICAL MODELING FRAMEWORK

3.1. Processing of μCT images

The proposed framework for modeling CB/UHMWPE nanocomposites is based on the μCT scans. First, initial volumetric images (TIFF format) are processed by performing cropping, smoothing, and leveling operations. Then, the produced images are binarized by assigning black color to UHMWPE granules and white color to the CB-containing layer. Finally, the binary images are cleaned from the noise to prepare them for statistical processing presented in the next subsection. The image processing procedure is illustrated in Fig. 3.

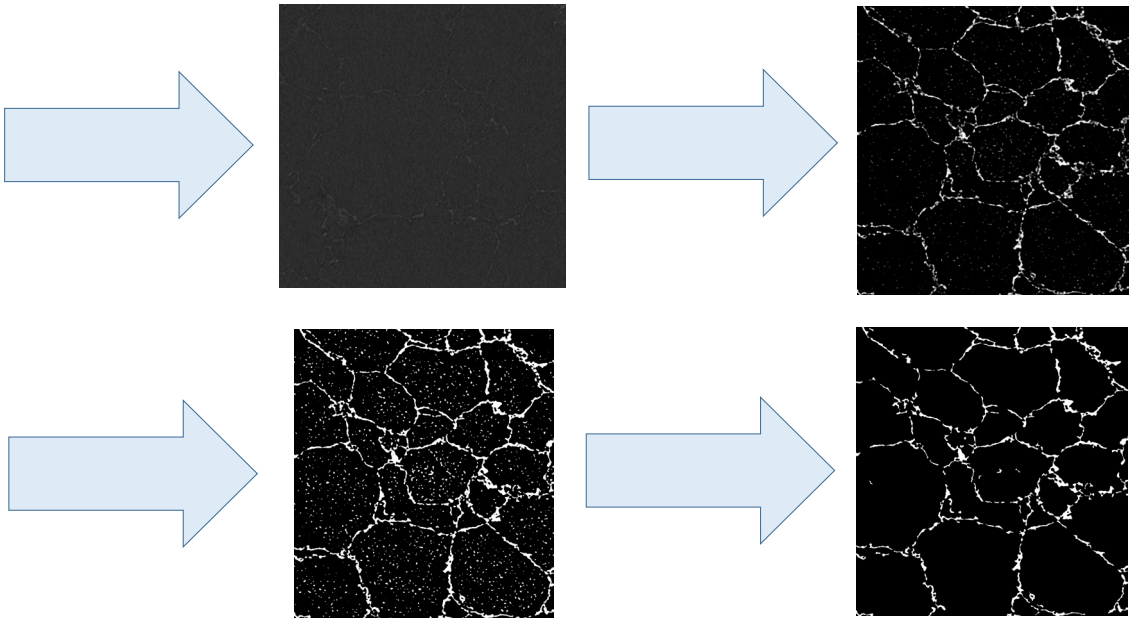

Fig.3: μCT image processing procedure for CB/UHMWPE nanocomposite.

3.2. Generation of statistically representative synthetic volume elements

The processed μCT images were used to generate statistically representative synthetic volume elements of CB/UHMWPE nanocomposite on the mesoscale. They are produced using two custom pipelines in the Dream3D open-source software (Groeber & Jackson, 2014). Pipeline 1 is responsible for the analysis and statistical processing of images. This customized pipeline extracts the size and shape of UHMWPE granules (sphericity, equivalent diameter, and the angle of the major axis) and then exports the data on each material feature in a CSV format. Pipeline 2 was developed for the construction of statistically similar synthetic volume elements using the processed feature statistics from Pipeline 1. The pipeline generates a synthetic volume, establishes shapes of granules, matches granule neighbors, and packs features in volume elements. The process results in a 3D model of the representative volume element (RVE), as illustrated in Fig.4. The CB-containing layer is introduced separately as follows: the Dream3D model of the RVE is exported to MATLAB as a structured VTK file. Then the interface surfaces between UHMWPE particles are identified and the interphase domain is introduced by layer-by-layer reassigning the boundary voxels until the desired thickness of the interphase domain is achieved. The process is controlled by the expected average thickness of the CB-containing layer, see (Miroshnichenko et al., 2023). An example of the resulting microstructure is shown in Fig. 4c. The RVE is a cube of 480^3 voxels with 8 to 10 voxels per CB-containing layer thickness.

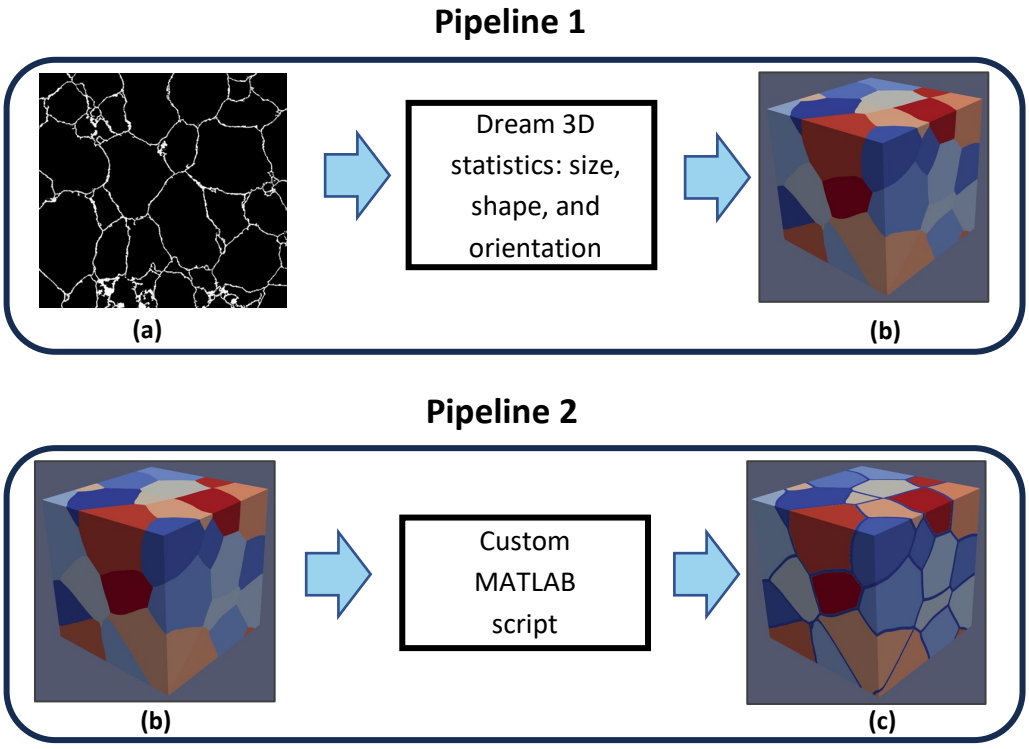

Fig.4: Generation of the CB/UHMWPE composite RVE: (a) μCT image, (b) statistically equivalent volume element, (c) RVE with CB-containing layer.

Finite element meshing of RVE is performed in MATLAB utilizing Iso2Mesh (Fang & Boas, 2009) open-source software. The volumetric images in the VTK format serve as an input to the internal Iso2mesh volumetric meshing procedure. The output of the procedure consists of an array of nodes and a tetrahedral mesh connectivity table with labels for the UHMWPE and CB-containing layer, respectively. This output requires additional processing, including regeneration and adjustment of the orientation of the elements on the RVE surface. This mesh is then exported to commercial Hexagon Marc (Marc 2019, https://hexagon.com/products/marc) software for FEA analysis. Fig. 5 illustrates FE meshes of the interphase domain and UHMWPE particles. The mesh is continuous through the RVE and its interphase domain. Several realizations of the RVE subdivided into ~1,000,000 linear tetrahedral elements were developed.

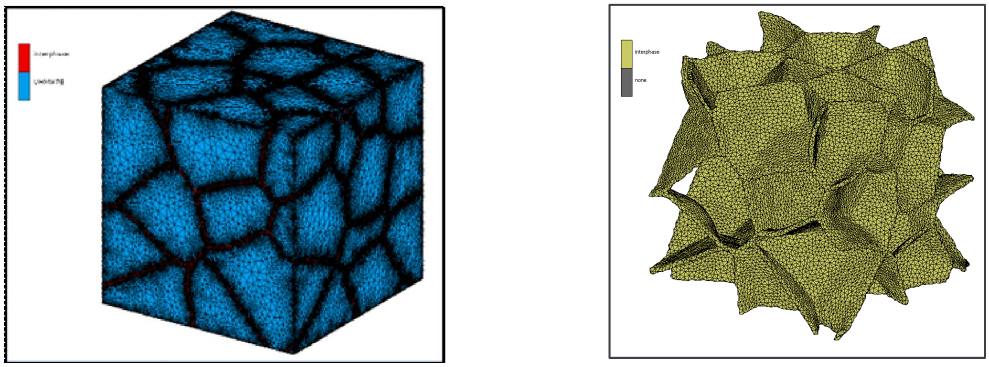

(a) (b)

Fig.5: Example of the RVE FE mesh for 10 wt% CB/UHMWPE nanocomposite: (a) RVE, (b) CB-containing layer. The total number of elements is ~1,600,000: UHMWPE phase – 839,000 elements, CB-containing layer – 761,000 elements. Depending upon the realization, at least 5 elements per thickness of the layer are introduced.

3.3. Micromechanical homogenization of CB-containing layer

The effective elastic properties of the CB-containing layer are predicted using micromechanical methods of continuum mechanics, both deterministic (Kachanov & Sevostianov, 2018) and probabilistic (Berdichevsky & Islam, 2024). The validity of continuum mechanics approaches for nanosize inclusions has been thoroughly discussed in the literature, justified by molecular dynamics simulations (Kushch, 2023; Odegard et al., 2005), and used in micromechanical modeling of nanocomposites with spherical inclusions (Janghorban & Rabczuk, 2024; Sevostianov & Kachanov, 2007). It is assumed that CB inclusions are of spherical shape (see (Spahr et al., 2017), randomly distributed, and perfectly bounded with UHMWPE in the CB-containing layer. Note that in the case of imperfect bonding, the approaches presented in (Kanaun, 2024; Kushch & Mogilevskaya, 2022; Lutz & Zimmerman, 1996; Sevostianov & Kachanov, 2007) are available. In the case of nonspherical shapes, the proper concentration parameter (stiffness of compliance contribution tensor) should be used, see (Sevostianov & Kachanov, 2015).

For low volume fraction of inclusions, one of the traditional micromechanical schemes (Self-consistent, Mori-Tanaka-Benveniste or Differential, see (Eroshkin & Tsukrov, 2005; Kachanov & Sevostianov, 2018)) can be used to predict the effective properties of the layer. However, in the range of volume fractions relevant to this study (up to 46%, see Table 1), the predictions diverge and become less accurate (Ghossein & Lévesque, 2012; Ju & Yanase, 2010). Comprehensive numerical studies presented by (Ghossein & Lévesque, 2012) show that the hybrid micromechanical model of Lielens (Lielens et al., 1998) is a better choice for the considered volume fraction range and stiffness contrast. Note that the study of Ghossein and Lévesque was conducted on spherical inhomogeneities, which is relevant to our case. When compared with their direct simulations, the error, for example, of the bulk modulus for 50% volume fraction of

inclusions and high contrast ($\frac{E_{inclusion}}{E_{matrix}} = 100$) was within 5-10% for Lielens scheme vs. 25-35% for Mori-Tanaka predictions.

The Lielens model can be presented in terms of the strain concentration factors as follows. First, the 4th-order strain concentration factor is introduced as the proportionality coefficient between the average strain in the inclusions $\boldsymbol{\varepsilon_I}$ and the macroscopic strain in the composite $\boldsymbol{\varepsilon}$ (Hill, 1963):

$$\boldsymbol{\varepsilon_I} = \boldsymbol{A}\colon\boldsymbol{\varepsilon} \tag{3}$$

Then, the effective stiffness of the composite is given by

$$\boldsymbol{C} = \boldsymbol{C_m} + V_i(\boldsymbol{C}_i - \boldsymbol{C}_m)\colon\boldsymbol{A} \tag{4}$$

For non-interacting ellipsoidal inclusions, the strain concentration tensor is expressed in terms of the Eshelby tensor $\boldsymbol{S}$ (Eshelby, 1957) as:

$$\boldsymbol{A} = [\boldsymbol{I} + \boldsymbol{S}\colon(\boldsymbol{C}_i)^{-1}\colon(\boldsymbol{C}_m - \boldsymbol{C}_i)]^{-1} \tag{5}$$

If the interaction of the inclusions cannot be neglected, one of the approaches would be to assume that each inclusion is subjected to the stress field modified by the presence of the other inclusions ((Benveniste, 1987; Mori & Tanaka, 1973). In this case, the effective stiffness tensor of the composite is expressed as

$$\boldsymbol{C} = \boldsymbol{C_m} + V_i(\boldsymbol{C}_i - \boldsymbol{C}_m)\colon(V_i\boldsymbol{I} + V_m\boldsymbol{A^{-1}})^{-1} \tag{6}$$

The Lielens scheme (Lielens et al., 1998) utilizes the Mori-Tanaka-Benveniste micromechanical formula with a modified strain concentration tensor $\boldsymbol{A_{LIL}}$. This tensor is chosen as an interpolation between the lower and upper bounds, corresponding to the inclusion material surrounded by the matrix material (Mori-Tanaka strain concentration) and the matrix material surrounded by the inclusion material (inverse Mori-Tanaka strain concentration). For the inverse Mori-Tanaka, the average strain in the matrix material is given by

$$\boldsymbol{\varepsilon} = [\boldsymbol{I} + \boldsymbol{S}\colon(\boldsymbol{C}_m)^{-1}\colon(\boldsymbol{C}_i - \boldsymbol{C}_m)]^{-1}\colon\boldsymbol{\varepsilon_I} \tag{7}$$

so that the strain concentration tensor obtained as (3) is

$$\boldsymbol{A_{inv}} = [\boldsymbol{I} + \boldsymbol{S}\colon(\boldsymbol{C}_m)^{-1}\colon(\boldsymbol{C}_i - \boldsymbol{C}_m)] \tag{8}$$

The interpolation coefficient was proposed by Lielens as $\frac{V_{c/L}+V_{c/L}{}^2}{2}$, providing the following strain concentration tensor

$$\boldsymbol{A_{LIL}} = \left[\left(1 - \frac{V_{c/L} + V_{c/L}^2}{2}\right)(\boldsymbol{A_{inv}})^{-1} + \frac{V_{c/L} + V_{c/L}^2}{2}(\boldsymbol{A})^{-1}\right]^{-1} \quad (9)$$

The effective stiffness is found by substituting (9) into (6).

Table 2 presents the effective Young's (E_{LIL}) and shear moduli (G_{LIL}) of the CB-containing layer for different weight fractions of CB considered in this paper. They are extracted from the effective stiffness tensor given by (11). The value of Young's modulus for the neat UHMWPE was determined by the Dynamic Mechanical Analysis (DMA), which is described in Section 4.2. For the CB particles, the value of $E_{CB} = 80GPa$ and $\nu_{CB} = 0.3$ suggested by (Jean et al., 2011) were used. Note that slightly different values of E for various types of CB (conductive, pigment, etc.) have been reported in the literature. However, CB is significantly stiffer than the UHMWPE, approaching the approximation of perfectly rigid inclusions and the predicted effective properties of the composite are not sensitive to the value of E_{CB} from the reported range.

TABLE 2**.** Effective elastic moduli of CB-containing layers

***CB* wt%**	$V_{c/L}$	E_{LIL} **[MPa]**	G_{LIL} **[MPa]**
0	0	920	329
0.5	0.35	2249	822
1	0.28	1823	664
1.5	0.29	1877	683
5	0.43	2938	1080
10	0.46	3277	1208

4. RESULTS AND DISCUSSION

4.1. Numerical modeling on mesoscale

To determine the effective elastic properties of CB/UHMWPE composite, FEM analysis of mesoscale RVEs was performed. Similar to the approach presented by (Drach et al., 2014; Ewert et al., 2020), six loadcases were applied to each RVE (three uniaxial tensions in mutually orthogonal directions and three shears), as presented in Table 3. In the Table, $X_1^+, X_1^-, X_2^+, X_2^-, X_3^+, X_3^-$ are the faces of the cubic volume element with outward normals directed in a positive or negative direction of the corresponding coordinate axes, a is the side length of the

representative volume cube, $\varepsilon^{(0)}$ is the value of applied strain, u_1, u_2, u_3 are the displacements in x_1, x_2, x_3 directions, correspondingly.

TABLE 3. Load cases to determine the effective elastic parameters of the composite

Loadcase 1 (uniaxial tension in x_1 direction): $X_1^- : u_1 = 0; \quad X_1^+ : u_1 = \varepsilon^{(0)} \cdot a;$ $X_1^-, X_1^+, X_2^-, X_2^+, X_3^-, X_3^+ : u_2 = 0; \quad u_3 = 0;$
Loadcase 2 (uniaxial tension in x_2 direction): $X_2^- : u_2 = 0; \quad X_2^+ : u_2 = \varepsilon^{(0)} \cdot a;$ $X_1^-, X_1^+, X_2^-, X_2^+, X_3^-, X_3^+ : u_1 = 0; \quad u_3 = 0;$
Loadcase 3 (uniaxial tension in x_3 direction): $X_3^- : u_3 = 0; \quad X_3^+ : u_3 = \varepsilon^{(0)} \cdot a;$ $X_1^-, X_1^+, X_2^-, X_2^+, X_3^-, X_3^+ : u_1 = 0; \quad u_2 = 0;$
Loadcase 4 (shear deformation in x_1x_2 plane): $X_1^- : u_2 = 0; \quad X_1^+ : u_2 = \varepsilon^{(0)} \cdot a;$ $X_1^-, X_1^+, X_2^-, X_2^+, X_3^-, X_3^+ : u_1 = 0; \quad u_3 = 0;$
Loadcase 5 (shear deformation in x_2x_3 plane): $X_2^- : u_3 = 0; \quad X_2^+ : u_3 = \varepsilon^{(0)} \cdot a;$ $X_1^-, X_1^+, X_2^-, X_2^+, X_3^-, X_3^+ : u_1 = 0; \quad u_2 = 0;$
Loadcase 6 (shear deformation in x_3x_1 plane): $X_3^- : u_1 = 0; \quad X_3^+ : u_1 = \varepsilon^{(0)} \cdot a;$ $X_1^-, X_1^+, X_2^-, X_2^+, X_3^-, X_3^+ : u_2 = 0; \quad u_3 = 0;$

Numerical simulations were performed in the Hexagon Marc commercial finite element package. The mesh consists of four-node tetrahedral elements with linear interpolation functions. The stiffness matrix is integrated using a single integration point at the centroid. Elements of the CB-containing layer are assigned to be perfectly bounded with UHMWPE granules. Figs. 6 and 7 illustrate distributions of the stresses in the RVE subjected to loadcase 1 and loadcase 4 correspondingly. In the simulations, $a = 350\mu m, \varepsilon^{(0)} = 0.001$.

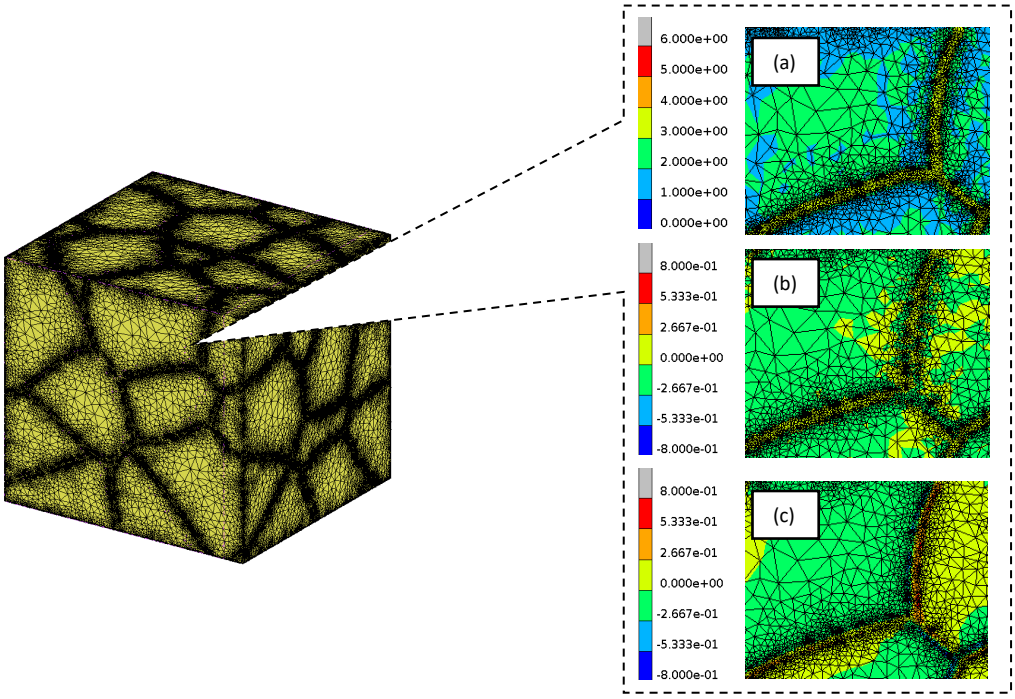

Fig.6: Selected stress fields (MPa) in the RVE of 5 wt% CB/UHMWPE nanocomposite subjected to loadcase 1: (a) σ_{11}, (b) σ_{12}, (c) σ_{13}.

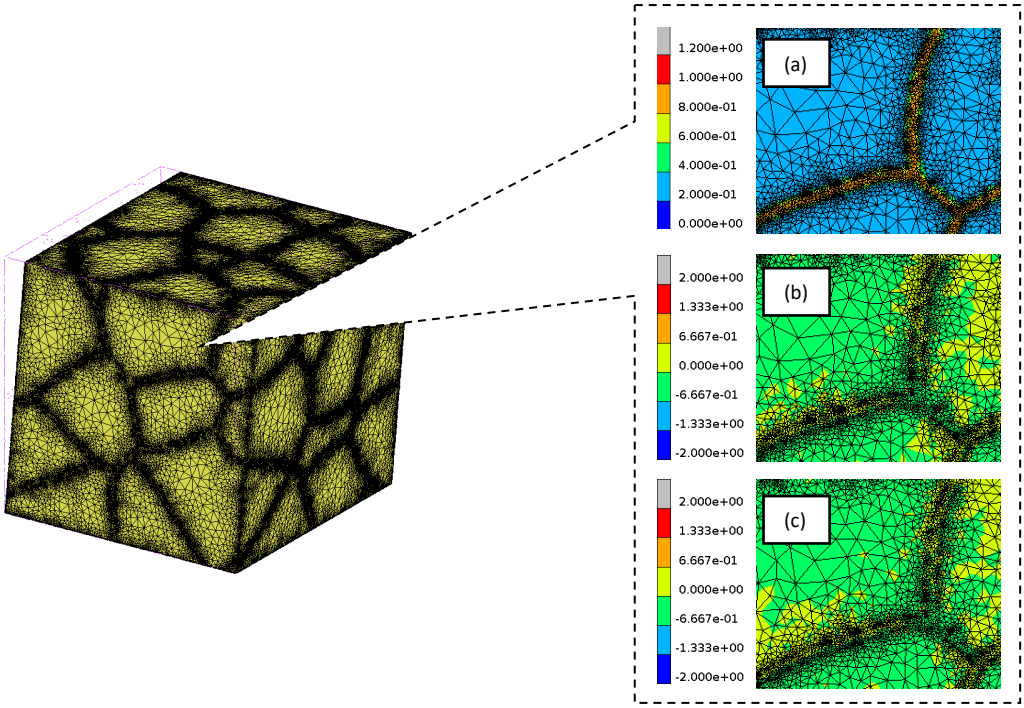

Fig.7: Selected stress (MPa) fields in the RVE of 5 wt% CB/UHMWPE nanocomposite subjected to loadcase 4: (a) σ_{12}, (b) σ_{11}, (c) σ_{22}.

A custom MATLAB data processing procedure was developed to process Marc numerical results. This procedure includes extraction of stress values from integration points of finite elements, extraction of nodes and their coordinates to calculate volumes of elements, and then volume averaging of stresses in the RVE:

$$\bar{\sigma}_{ij} = \frac{1}{V}\sum_{l=1}^{N} \sigma_{ij}^{(l)} V^{(l)}, \qquad i,j = 1,2,3 \tag{10}$$

where $\sigma_{ij}^{(l)}$ is the stress value of l's element, $V^{(l)}$ is the volume of the l's element, N is the number of finite elements in the model.

The effective elastic parameters of the material are then extracted from the compliance matrix that relates the components of the average stress ($\bar{\sigma}_{ij}$) and applied strain ($\bar{\varepsilon}_{ij}$):

$$\begin{Bmatrix} \bar{\varepsilon}_{11} \\ \bar{\varepsilon}_{22} \\ \bar{\varepsilon}_{33} \\ \bar{\varepsilon}_{23} \\ \bar{\varepsilon}_{31} \\ \bar{\varepsilon}_{12} \end{Bmatrix} = \begin{bmatrix} 1/E_1 & -v_{21}/E_2 & -v_{31}/E_3 & 0 & 0 & 0 \\ -v_{12}/E_1 & 1/E_2 & -v_{32}/E_3 & 0 & 0 & 0 \\ -v_{13}/E_1 & -v_{23}/E_2 & 1/E_3 & 0 & 0 & 0 \\ 0 & 0 & 0 & 1/G_{23} & 0 & 0 \\ 0 & 0 & 0 & 0 & 1/G_{31} & 0 \\ 0 & 0 & 0 & 0 & 0 & 1/G_{12} \end{bmatrix} . \begin{Bmatrix} \bar{\sigma}_{11} \\ \bar{\sigma}_{22} \\ \bar{\sigma}_{33} \\ \bar{\sigma}_{23} \\ \bar{\sigma}_{31} \\ \bar{\sigma}_{12} \end{Bmatrix} \tag{11}$$

Note that we expect the response of the composite to be isotropic. However, to evaluate the accuracy of the FEM meshing (absence of the bias due to the selected meshing procedure) and confirm that the RVE is statistically representative (contains enough UHMWPE granules), the orthotropic elastic parameters were extracted separately and compared with the average values for all considered RVEs. This information is included in the error bars of the presented numerical modeling results reported in Section 4.2.

4.2. Dynamic Mechanical Analysis of selected specimens

The mechanical properties of virgin GUR1050 UHMWE matrix material and CB/UHMWPE composite were determined by DMA. The 15 x 4.1 x 0.5 mm^3 specimens were cut from the bulk material manufactured by CM as described in Section 2.1. A Q800 DMA (TA Instruments, New Castle, DE) was used to analyze the loss and storage moduli of the composite CB/UHMWPE samples. The gauge lengths of the samples between the DMA clamps varied between 9 -12 mm. After a five-minute isothermal equilibration time at 35°C, the samples were swept from 1 to 30 Hz by increasing the frequency to collect 40 data points. An oscillating strain of 0.2% was applied to the sample under 0.01 N of preload force. A total of 6 samples per weight fraction of CB in the composite were made for both CM and ECAE manufactured materials.

DMA testing of the neat UHMWPE determined the average tensile storage modulus $E' = 920\,MPa$ and tensile loss modulus $E'' = 37\,MPa$. These results show that for pure

UHMWPE the loss modulus can be neglected, and the material's behavior can be considered purely elastic with elastic modulus $E = 920\ MPa$. This value can be combined with the known Poisson's ratio of 0.4 (Lu et al., 2021) to evaluate the shear modulus of the neat UHMWPE as $G = 330MPa$. The averaged values of Young's modulus of the CB/UHMWPE composites determined with DMA are presented in Fig.8 as diamond-shaped points with the corresponding error bars.

4.3 Predictions of the overall elastic parameters of CB/UHMWPE nanocomposites

Numerical estimates of the effective Young's and shear moduli as functions of wt% fraction of CB inclusions are shown in Figs. 8, 9, and Table 4. Fig. 8 also provides a comparison with the experimental data obtained by DMA in Section 4.2. The numerical predictions of effective elastic parameters are shown as green circles connected by solid lines. Each data point is the average of all orthotropic Young's moduli for 3 RVEs (a total of 9 data points). The standard deviation *S* is calculated as:

$$S = \sqrt{\frac{\sum(E_i - E_{avg})^2}{N}}, \qquad i = 1,2,3 \tag{12}$$

where E_i are the values of the orthotropic elastic moduli from numerical simulation, E_{avg} is the average Young's modulus, and *N* is the number of data points in the population. This standard deviation is shown as error bars on the graphs and presented in Table 4. The small standard deviation values (less than 8 MPa) suggest that the overall material is macroscopically isotropic, and the number of included UHMWPE granules is sufficient for the statistical representation of the material. Note that our mesoscale numerical models of RVE included approximately 40 granules, which is of the same order as used in (Li & Ma, 2022).

Table 4. Numerical predictions for the effective Young's and shear moduli of the CB/UHMWPE composite. Mean values and standard deviations.

wt% of CB	E (MPa)	G (MPa)	E std (MPa)	G std (MPa)
0	920	330	-	-
0.5	926	331	6.3	0.2
1	930	332	6.1	0.2
1.5	935	334	5.8	0.1
2.5	945	338	5.3	0.2
5	977	349	4.1	0.6
7.5	1023	366	3.5	1.7
10	1100	394	8.3	3.8

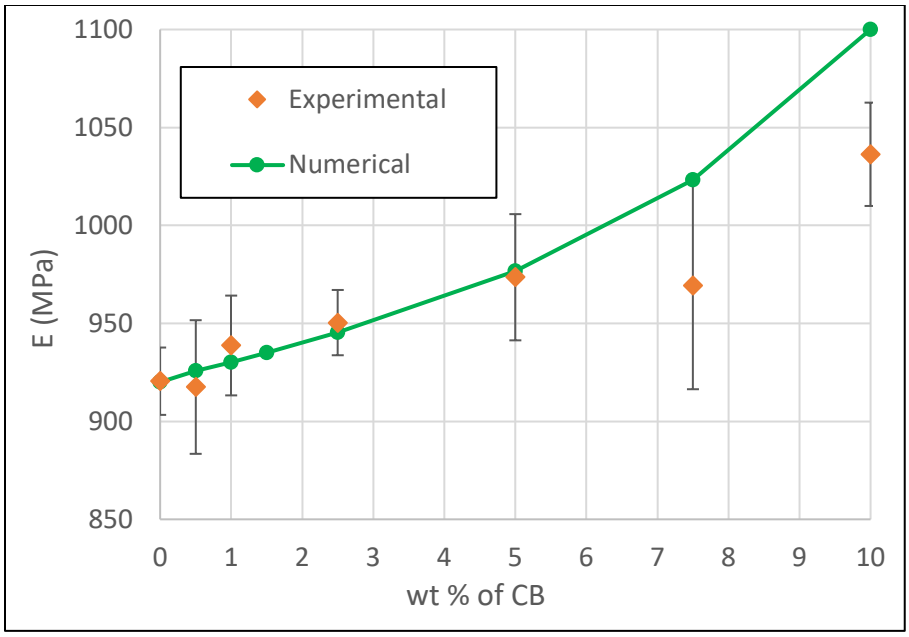

Fig. 8: Effective Young's modulus of the CB/UHMWPE nanocomposite: numerical predictions vs. experimental measurements. Note that the numerical results are included with the error bars that are not visible as their size is smaller than the data point marker.

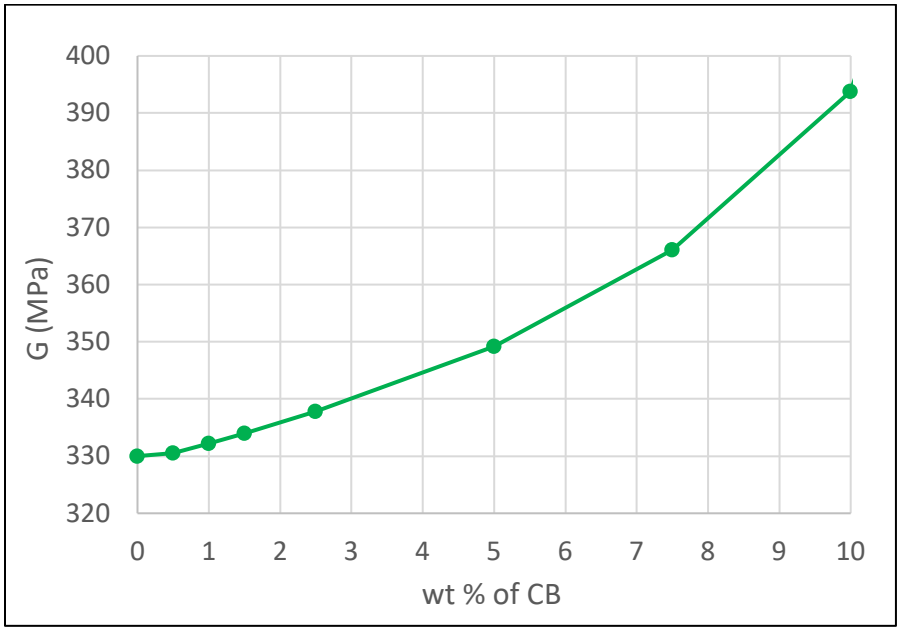

Fig. 9: Effective shear modulus predictions for the CB/UHMWPE nanocomposite.

It is observed that for the range of up to 5 wt% fractions of CB inclusions the numerical predictions lie within the confidence intervals of the experimental measurements. As expected, the elastic moduli of the composite (both *E* and *G*) increase with the increase of concentration of stiff

CB particles. For 10 wt% of CB, the numerical predictions for Young's modulus are 6% higher than the experimental value. A potential reason for this discrepancy is the formation of clusters of CB inclusions that inhibits load transfer between constituents and violates the assumptions of random distribution and perfect bonding of the inclusions within the CB-containing layer, as illustrated in Fig. 10.

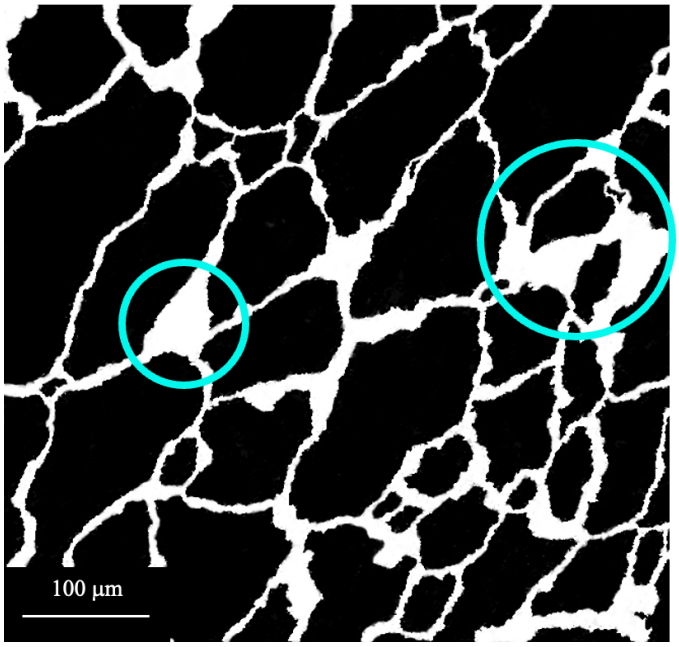

Fig.10: Example of a μCT image of 10 wt% CB/UHMWPE composite with clusters of CB.

4.4 Applicability to other material systems

The applicability of the modeling approach proposed in this paper is not limited to the considered type of CB/UHMWPE nanocomposites. The approach of the inclusions-containing layer can be used for numerical modeling of other material systems with similar microstructure features. For example, studies conducted by (Favreau et al., 2022) and (Miroshnichenko et al., 2023) demonstrate that similar microstructure and spatial distribution are also observed in ultra-high-molecular-weight-polyethylene-based nanocomposites with nanographite inclusions. In that case, the Eshelby tensor for highly oblate spheroidal shape (penny shape inclusion) should be used in the micromechanical formulas (5) and (8) for the carbon-containing layer. A thorough review of the available modeling methods for nanographene-doped materials can be found in (Yee & Ghayesh, 2023).

Another class of material systems relevant to the proposed modeling approach is drug-eluting polymers. In particular, UHMWPE with antibacterial and anesthetic additives was investigated in (Gil et al., 2019; Grindy et al., 2019; Lekkala et al., 2024) for joint replacement applications. If the

shape and the spatial distribution of drug inclusions are known, the Lielens micromechanical scheme, considered in this paper, could be used to predict the effective mechanical properties of the resulting composite.

5. CONCLUSIONS

In this paper, Carbon-Black/UHMWPE nanocomposites are studied by X-ray micro-computed tomography, and the effective elastic properties are predicted by mesoscale numerical models. The models take into account the complex microstructure of the composite by incorporating an inclusion-containing layer (CB-containing layer) homogenized by an analytical micromechanical scheme. This approach can be used for other composites with similar spatial distribution of inclusions of various types and shapes. The following conclusions can be made.

- Carbon-Black/UHMWPE composites exhibit complex microstructure with UHMWPE granules surrounded by CB-containing layers. μCT analysis shows that for considered weight fractions (0-10%) of CB, the volume fraction of the CB-containing layer can reach up to 11.2% with the volume fraction of CB inclusions in the layer approaching 50%.

- Analytical micromechanical modeling can be used to estimate the effective elastic stiffness of the CB-containing layers. Utilizing the DMA-determined stiffness of the bulk UHMWPE, the effective Young's modulus of the CB-containing layer was estimated as varying between 2.2 and 3.3 GPa.

- The CB-containing layers can be incorporated in mesoscale FEM models of representative volume elements using the framework presented in Section 3.2 of this paper. The framework utilizes the μCT images to extract the statistics on the spatial distribution and shape of UHMWPE granules and incorporates the CB-containing layers to the RVEs generated based on the observed statistics.

- Finite element simulations of 6 basic loadcases (uniaxial and shear loading in 3 orthogonal directions) allow the extraction of the overall elastic moduli of the composite. The paper reports the values of Young's and shear moduli for 0.5%, 1%, 2.5%, 5%, 7.5% and 10 wt%. fractions of CB inclusions.

- Comparison of the numerical simulations results with the experimental measurements of Young's modulus on the specimens manufactured by compression molding and equal channel angular extrusion techniques shows that numerical results fall within the standard deviations of the experimental data up to 5 wt% of CB inclusions. For higher CB concentrations, the

numerical model overpredicts the stiffness potentially due to the formation of CB clusters within the CB-containing layers.

6. ACKNOWLEDGEMENTS

The authors acknowledge funding by the National Science Foundation NH BioMade EPSCoR award (#1757371). X-ray microscopy research is supported by the Center of Integrated Biomedical and Bioengineering Research through a grant from the National Institute of General Medical Sciences (P20GM113131) at the National Institutes of Health.

7. REFERENCES

Armbrister, C. E. E., Okoli, O. I., & Shanbhag, S. (2015). Micromechanics predictions for two-phased nanocomposites and three-phased multiscale composites: A review. *Journal of Reinforced Plastics and Composites*, *34*(8), 605–613. https://doi.org/10.1177/0731684415574297

Asbury Carbon, 2024. https://www.asburystore.com/v/vspfiles/templates/174/pdf/5345R_PDS.pdf, accessed on 9/20/2024.

Baliga, B. R., Reddy, P., & Pandey, P. (2018). Synthesis and Wear Characterization of CNF-UHMWPE Nanocomposites for Orthopaedic Applications. *Materials Today: Proceedings*, *5*(10), 20842–20848. https://doi.org/10.1016/J.MATPR.2018.06.470

Beloshenko, V. A., Voznyak, Y. V., Reshidova, I. Y., Naït-Abdelaziz, M., & Zairi, F. (2013). Equal-channel angular extrusion of polymers. *Journal of Polymer Research*, *20*(12). https://doi.org/10.1007/S10965-013-0322-2

Benveniste, Y. (1987). A new approach to the application of Mori-Tanaka's theory in composite materials. *Mechanics of Materials*, *6*(2), 147–157. https://doi.org/10.1016/0167-6636(87)90005-6

Berdichevsky, V. L., & Islam, M. T. (2024). The variational principle for probabilistic measure and Hashin–Shtrikman bounds. *International Journal of Engineering Science*, *196*. https://doi.org/10.1016/j.ijengsci.2023.104015

BUKLOVSKYI, S., MIROSHNICHENKO, K., TSUKROV, I., THOMSON, R. J., SOLBERG, P. C., & CITTERS, D. W. VAN. (2023). Prediction of Effective Elastic Properties of Carbon/UHMWPE Nanocomposites by Combination of Numerical and Analytical Modeling. *PROCEEDINGS OF THE AMERICAN SOCIETY FOR COMPOSITES-THIRTY-EIGHTH TECHNICAL CONFERENCE*, *0*(0). https://doi.org/10.12783/ASC38/36636

Clark, A. C., Ho, S. P., & LaBerge, M. (2006). Conductive composite of UHMWPE and CB as a dynamic contact analysis sensor. *Tribology International*, *39*(11), 1327–1335. https://doi.org/10.1016/J.TRIBOINT.2005.10.004

Cook, D. J., Chun, H. H., & Van Citters, D. W. (2019). Mechanical and Electrical Characterization of Two Carbon/Ultra High Molecular Weight Polyethylene Composites Created Via Equal Channel Angular Processing. *Journal of Engineering Materials and Technology, Transactions of the ASME*, *141*(2). https://doi.org/10.1115/1.4041389/366885

Drach, A., Drach, B., & Tsukrov, I. (2014). Processing of fiber architecture data for finite element modeling of 3D woven composites Dedicated to Professor Zdeněk Bittnar in occasion of his 70th birthday. *Advances in Engineering Software*, *72*, 18–27. https://doi.org/10.1016/j.advengsoft.2013.06.006

Eroshkin, O., & Tsukrov, I. (2005). On micromechanical modeling of particulate composites with inclusions of various shapes. *International Journal of Solids and Structures*, *42*(2), 409–427. https://doi.org/10.1016/J.IJSOLSTR.2004.06.045

Eshelby, J. D. (1957). The Determination of the Elastic Field of an Ellipsoidal Inclusion, and Related Problems. In *Source: Proceedings of the Royal Society of London. Series A, Mathematical and Physical Sciences* (Vol. 241, Issue 1226). https://www.jstor.org/stable/100095

Ewert, A., Drach, B., Vasylevskyi, K., & Tsukrov, I. (2020). Predicting the overall response of an orthogonal 3D woven composite using simulated and tomography-derived geometry. *Composite Structures*, *243*. https://doi.org/10.1016/j.compstruct.2020.112169

Fang, Q., & Boas, D. A. (2009). *TETRAHEDRAL MESH GENERATION FROM VOLUMETRIC BINARY AND GRAY-SCALE IMAGES*.

Favreau, H. J., Miroshnichenko, K. I., Solberg, P. C., Tsukrov, I. I., & Van Citters, D. W. (2022). Shear enhancement of mechanical and microstructural properties of synthetic graphite and ultra-high molecular weight polyethylene carbon composites. *Journal of Applied Polymer Science*, *139*(20), 52175. https://doi.org/10.1002/APP.52175

Ghossein, E., & Lévesque, M. (2012). A fully automated numerical tool for a comprehensive validation of homogenization models and its application to spherical particles reinforced composites. *International Journal of Solids and Structures*, *49*(11–12), 1387–1398. https://doi.org/10.1016/j.ijsolstr.2012.02.021

Gil, D., Grindy, S., Muratoglu, O., Bedair, H., & Oral, E. (2019). Antimicrobial effect of anesthetic-eluting ultra-high molecular weight polyethylene for post-arthroplasty antibacterial prophylaxis. *Journal of Orthopaedic Research*, *37*(4), 981–990. https://doi.org/10.1002/JOR.24243

Grindy, S. C., Gil, D., Suhardi, J. V., Muratoglu, O. K., Bedair, H., & Oral, E. (2019). Delivery of bupivacaine from UHMWPE and its implications for managing pain after joint arthroplasty. *Acta Biomaterialia*, *93*, 63–73. https://doi.org/10.1016/J.ACTBIO.2019.05.049

Groeber, M. A., & Jackson, M. A. (2014). DREAM.3D: A Digital Representation Environment for the Analysis of Microstructure in 3D. *Integrating Materials and Manufacturing Innovation*, *3*(1), 56–72. https://doi.org/10.1186/2193-9772-3-5/FIGURES/6

Hill, R. (1963). Elastic properties of reinforced solids: Some theoretical principles. *Journal of the Mechanics and Physics of Solids*, *11*(5), 357–372. https://doi.org/10.1016/0022-5096(63)90036-X

Hunt, B. J., & Joyce, T. J. (2016). A tribological assessment of Ultra High Molecular Weight Polyethylene types GUR 1020 and GUR 1050 for orthopedic applications. *Lubricants*, *4*(3). https://doi.org/10.3390/lubricants4030025

Janghorban, M., & Rabczuk, T. (2024). Study of nanotube waviness influence on the behaviors of spherical nanocomposites. *International Journal of Engineering Science*, *199*. https://doi.org/10.1016/j.ijengsci.2024.104059

Jean, A., Willot, F., Cantournet, S., Forest, S., Jeulin, D., Jean, A., Willot, F., Cantournet, S., Forest, S., & Jeulin, D. (2011). Large-scale computations of effective elastic properties of rubber with carbon black fillers. *International Journal for Multiscale Computational Engineering*, *9*, 271–303. https://doi.org/10.1615/IntJMultCompEng.v9.i3.30ï

Ju, J. W., & Yanase, K. (2010). Micromechanics and effective elastic moduli of particle-reinforced composites with near-field particle interactions. *Acta Mechanica*, *215*(1–4), 135–153. https://doi.org/10.1007/s00707-010-0337-2

Kachanov, M., & Sevostianov, I. (2018). *Micromechanics of Materials, with Applications*. *249*. https://doi.org/10.1007/978-3-319-76204-3

Kanaun, S. (2024). Radially transverse isotropic inclusions in isotropic elastic media: Local fields, neutral inclusions, effective elastic properties. *International Journal of Engineering Science*, *200*, 104078. https://doi.org/10.1016/j.ijengsci.2024.104078

Kushch, V. I. (2023). Atomistic and continuum modeling of nanoparticles: Elastic fields, surface constants, and effective stiffness. *International Journal of Engineering Science*, *183*. https://doi.org/10.1016/j.ijengsci.2022.103806

Kushch, V. I., & Mogilevskaya, S. G. (2022). On modeling of elastic interface layers in particle composites. *International Journal of Engineering Science*, *176*. https://doi.org/10.1016/J.IJENGSCI.2022.103697

Lekkala, S., Inverardi, N., Grindy, S. C., Hugard, S., Muratoglu, O. K., & Oral, E. (2024). Irradiation Behavior of Analgesic and Nonsteroidal Anti-Inflammatory Drug-Loaded UHMWPE for Joint Replacement. *Biomacromolecules*. https://doi.org/10.1021/acs.biomac.3c01179

Li, Y., & Ma, C. (2022). A multiscale computational framework for wear prediction in knee replacement implants. *Mechanics of Materials*, *175*. https://doi.org/10.1016/j.mechmat.2022.104480

Lielens, G., Pirotte, P., Couniot, A., Dupret, F., & Keunings, R. (1998). Prediction of thermo-mechanical properties for compression moulded composites. In *Composites Purt A* (Vol. 29).

Lu, X., Meng, Q., & Jin, Z. (2021). Effects of UHMWPE viscoelasticity on the squeeze-film lubrication of hip replacements. *Biosurface and Biotribology*, *7*(2), 60–69. https://doi.org/10.1049/BSB2.12006

Lutz, M. P., & Zimmerman, R. W. (1996). Effect of the Interphase Zone on the Bulk Modulus of a Particulate Composite. *Journal of Applied Mechanics*, *63*(4), 855–861. https://doi.org/10.1115/1.2787239

Miroshnichenko, K., Buklovskyi, S., Vasylevskyi, K., Tsukrov, I., Favreau, H. J., Thomson, R. J., Solberg, P. C., & Van Citters, D. W. (2023). Characterization and modeling of carbon black/ultra-high-molecular-weight-polyethylene nanocomposites manufactured with equal channel angular extrusion. *AIP Conference Proceedings*, *2848*(1). https://doi.org/10.1063/5.0145202/2895672

Mori, T., & Tanaka, K. (1973). Average stress in matrix and average elastic energy of materials with misfitting inclusions. *Acta Metallurgica*, *21*(5), 571–574. https://doi.org/10.1016/0001-6160(73)90064-3

Odegard, G. M., Valavala, P. K., & Odegard, G. M. (2005). *Modeling techniques for determination of mechanical properties of polymer nanocomposites*. https://www.researchgate.net/publication/228353352

Park, C. H., & Lee, W. I. (2012). Compression molding in polymer matrix composites. *Manufacturing Techniques for Polymer Matrix Composites (PMCs)*, 47–94. https://doi.org/10.1533/9780857096258.1.47

Reddy, S. K., Kumar, S., Varadarajan, K. M., Marpu, P. R., Gupta, T. K., & Choosri, M. (2018). Strain and damage-sensing performance of biocompatible smart CNT/UHMWPE nanocomposites. *Materials Science and Engineering C*, *92*, 957–968. https://doi.org/10.1016/j.msec.2018.07.029

Reinitz, S. D., Engler, A. J., Carlson, E. M., & Van Citters, D. W. (2016). Equal channel angular extrusion of ultra-high molecular weight polyethylene. *Materials Science & Engineering. C, Materials for Biological Applications*, *67*, 623–628. https://doi.org/10.1016/J.MSEC.2016.05.085

Rothammer, B., Marian, M., Neusser, K., Bartz, M., Böhm, T., Krauß, S., Schroeder, S., Uhler, M., Thiele, S., Merle, B., Kretzer, J. P., & Wartzack, S. (2021). Amorphous Carbon Coatings for Total Knee Replacements—Part II: Tribological Behavior. *Polymers*, *13*(11). https://doi.org/10.3390/POLYM13111880

Segal, V. M. (1999). Equal channel angular extrusion: from macromechanics to structure formation. *Materials Science and Engineering: A*, *271*(1–2), 322–333. https://doi.org/10.1016/S0921-5093(99)00248-8

Sevostianov, I., & Kachanov, M. (2007). Effect of interphase layers on the overall elastic and conductive properties of matrix composites. Applications to nanosize inclusion. *International Journal of Solids and Structures*, *44*(3–4), 1304–1315. https://doi.org/10.1016/j.ijsolstr.2006.06.020

Sevostianov, I., & Kachanov, M. (2015). On the possibility to represent effective properties of a material with inhomogeneities in terms of concentration parameters. *International Journal of Solids and Structures*, *52*, 197–204. https://doi.org/10.1016/J.IJSOLSTR.2014.10.003

Solberg, P.C. (2024) Application-Driven Materials Development of Solid-State Conductive Composites of Ultra-High Molecular Weight Polyethylene. *Ph.D. dissertation*, Dartmouth University, NH USA.

Spahr, M. E., Gilardi, R., & Bonacchi, D. (2017). *Carbon Black for Electrically Conductive Polymer Applications*. 375–400. https://doi.org/10.1007/978-3-319-28117-9_32

Staniszewski, J. M., Boyd, S. E., & Bogetti, T. A. (2022). A multi-scale modeling approach for UHMWPE composite laminates with application to low-velocity impact loading. *International Journal of Impact Engineering*, *159*. https://doi.org/10.1016/j.ijimpeng.2021.104031

Sui, G., Zhong, W. H., Ren, X., Wang, X. Q., & Yang, X. P. (2009). Structure, mechanical properties and friction behavior of UHMWPE/HDPE/carbon nanofibers. *Materials Chemistry and Physics*, *115*(1), 404–412. https://doi.org/10.1016/j.matchemphys.2008.12.016

Thomson, R. J., Limberg, A. K., & Van Citters, D. W. (2023). Nanoparticles in Joint Arthroplasties. *Nano LIFE*, *13*(01). https://doi.org/10.1142/S1793984423300017

Vasylevskyi, K., Tsukrov, I., Miroshnichenko, K., Buklovskyi, S., Grover, H., & Van Citters, D. (2021). Finite Element Model of Equal Channel Angular Extrusion of Ultra High Molecular Weight Polyethylene. *Journal of Manufacturing Science and Engineering, Transactions of the ASME*, *143*(12). https://doi.org/10.1115/1.4051189/1109387

Wypych, G. (2014). Carbon black. *Databook of Antistatics*, 245–271. https://doi.org/10.1016/B978-1-895198-61-4.50007-9

Yee, K., & Ghayesh, M. H. (2023). A review on the mechanics of graphene nanoplatelets reinforced structures. *International Journal of Engineering Science*, *186*, 103831. https://doi.org/10.1016/J.IJENGSCI.2023.103831

Zeng, Q. H., Yu, A. B., & Lu, G. Q. (2008). Multiscale modeling and simulation of polymer nanocomposites. *Progress in Polymer Science*, *33*(2), 191–269. https://doi.org/10.1016/J.PROGPOLYMSCI.2007.09.002

Zoo, Y.-S., An, J.-W., Lim, D.-P., & Lim, D.-S. (2004). *Effect of carbon nanotube addition on tribological behavior of UHMWPE*.